IOP Publishing Journal of Physics D: Applied Physics
J. Phys. D: Appl. Phys. **50** (2017) 135202 (14pp) https://doi.org/10.1088/1361-6463/aa5c1d

2D modeling and simulation of the flow dynamics, electric field and reactions in a low-temperature, atmospheric-pressure nitrogen plasma sharp-end plate-to-plane configuration and CVD reactor

Juray De Wilde[1], Christophe Lorant[1] and Pierre Descamps[2]

[1] Materials and Process Engineering (IMAP), Université catholique de Louvain, Place Sainte Barbe 2, B-1348 Louvain-la-Neuve, Belgium
[2] Dow Corning, Solar Cell S&T Research, Seneffe, Belgium

E-mail: juray.dewilde@uclouvain.be

Received 14 September 2016, revised 19 January 2017
Accepted for publication 25 January 2017
Published 1 March 2017

Abstract

In atmospheric-pressure plasma reactors, the flow dynamics can be complex, determine the reactor performance and complicate scale-up. Coupling computational fluid dynamics to the calculation of the electric field and plasma chemistry is challenging because of the numerical stiffness introduced by the difference in time scale of the different phenomena involved. Focusing on low-temperature, atmospheric-pressure pure nitrogen plasma, a model and model reduction based solution strategy to deal with the numerical stiffness are presented and evaluated. The influence of the electric field on the flow dynamics and species concentration fields is first qualitatively studied by means of 2D simulations of a sharp-end plate-to-plane configuration. Next, a specific reactor prototype for low-temperature, atmospheric-pressure plasma-enhanced chemical vapor deposition for in-line surface treatments is simulated to illustrate the importance of accounting for the detailed flow dynamics.

Keywords: atmospheric-pressure plasma, flow dynamics, plasma simulation, (plasma enhanced) chemical vapor deposition, modelling in line reactor prototype, APPECVD

(Some figures may appear in colour only in the online journal)

Symbols

Latin letters

$C(f_e)$	Change rate of f_e (1/s)
D_i	Diffusivity of ionic species i ($m^2\,s^{-1}$)
D_A	Diffusivity of $N_2(A)$ ($m^2\,s^{-1}$)
D_n^{eff}	Effective diffusivity of neutral species n ($m^2\,s^{-1}$)
D_e	Diffusivity of electrons ($m^2\,s^{-1}$)
$\overline{E}$	Electric field ($V\,m^{-1}$)
f_e	Electron energy distribution function (—)
$\overline{g}$	Gravity vector ($m\,s^{-2}$)
H	Specific gas phase energy ($J\,kg^{-1}$)
h_e	Air to external wall heat transfer coefficient ($W\,m^{-2}\cdot K^{-1}$)
h_g	Process gas to inner wall heat transfer coefficient ($W\,m^{-2}\cdot K^{-1}$)
$\overline{j}_s$	Secondary electron emission current ($1/m^2\cdot s$)
k_B	Boltzmann constant ($J\,K^{-1}$)
M_j	Molar mass of species j ($kg\,mol^{-1}$)
M_n	Molar mass of neutral species n ($kg\,mol^{-1}$)
m_e	Electron mass (kg)

$\overline{n}$	Unit vector normal to the surface (—)
n_e	Electron density ($1/m^3$)
n_i	Density of ionic species i ($1/m^3$)
$n_{N_2(A)}$	Density of excited state $A^3\Sigma_u^+$ ($1/m^3$)
p^{eff}	Effective pressure (Pa)
q_e	Electron charge (C)
q_i	Charge of ionic species i (C)
$\overline{q}_w$	Heat flux at the wall ($W\,m^{-2}$)
R_k	Rate of reaction k ($mol\,m^{-3}\cdot s^{-1}$)
S_j	Source term of species j ($kg\,m^{-3}\cdot s^{-1}$)
S_e	Source term for electrons ($kg\,m^{-3}\cdot s^{-1}$)
S_i	Source term for ionic species i ($kg\,m^{-3}\cdot s^{-1}$)
T_g	Gas phase temperature (K)
T_{wg}	Wall temperature, inner side (K)
T_{we}	Wall temperature, outer side (K)
T_∞	Air temperature outside the reactor (K)
T_e	Electronic temperature (K)
t	Time (s)
$\overline{u}$	Velocity vector ($m\,s^{-1}$)
$\overline{u}_e$	Electron velocity ($m\,s^{-1}$)
$\overline{u}_i$	Ion velocity ($m\,s^{-1}$)
$x_{N_2(A)}$	$N_2(A)$ mass fraction (—)
x_j	Mass fraction of species j (—)
x_i	Mass fraction of ionic species i (—)
x_n	Mass fraction of neutral species n (—)
x_e	Electron mass fraction (—)

Greek letters

α_{jk}	Stoichiometric coefficient of species j in reaction k (—)
α_r	Rate constant for recombination reactions (m^3 ($kmol^{-1}\cdot s^{-1}$))
$\overline{\Gamma}_j$	Mass flux of species j ($kg\,m^{-2}\cdot s^{-1}$)
$\overline{\Gamma}_e$	Mass flux of electron ($kg\,m^{-2}\cdot s^{-1}$)
$\overline{\Gamma}_i$	Mass flux of ionic species i ($kg\,m^{-2}\cdot s^{-1}$)
$\overline{\Gamma}_n$	Mass flux of neutral species n ($kg\,m^{-2}\cdot s^{-1}$)
γ	Ion secondary electron emission coefficient (—)
γ_m	Metastable species secondary electron emission coefficient (—)
$\overline{\gamma}_p$	Photon secondary electron emission coefficient ($1/m^2\cdot s$)
ϵ_e	Electron mean energy (J)
ϵ_0	Dielectric constant ($F\,m^{-1}$)
θ	Reduced electric field (Td) $= (10^{-21}\,V\,m^2)$
λ_w	Thermal conductivity of the wall ($W\,m^{-1}\cdot K^{-1}$)
λ_g^{eff}	Effective thermal conductivity of the gas ($W\,m^{-1}\cdot K^{-1}$)
$\mu_{el,i}$	Electrical mobility of ionic species i ($V\,m^2\,s^{-1}$)
$\mu_{el,e}$	Electrical mobility of electrons ($V\,m^2\,s^{-1}$)
μ_g^{eff}	Effective gas viscosity ($kg\,m^{-1}\cdot s^{-1}$)
ρ_g	Gas density ($kg\,m^{-3}$)
ρ_{el}	Charge density ($C\,m^{-3}$)
Φ	Voltage (V)
$\overline{\overline{\tau}}_g^{eff}$	Effective shear stress tensor (Pa)

1. Introduction

For the past 20 years, interest in atmospheric pressure plasma discharges for industrial applications has been growing steadily (Schütze *et al* 1998, Bogaerts *et al* 2002, Aubry *et al* 2005, Tendero *et al* 2006, Massines *et al* 2008, Ravasio and Cavallotti 2012). They are used in various processes, such as atmospheric-pressure plasma-enhanced chemical vapor deposition (APPECVD) (Barranco *et al* 2001, Foest *et al* 2003, Massines *et al* 2005, Enache *et al* 2007), a technique allowing fast and inline treatment of wide surfaces while avoiding the use of vacuum system. This makes APPECVD highly attractive when there is a need for increased production rates and reduced production costs, for example in the solar panel market. Low temperature plasmas, also referred as non-thermal plasmas, are of particular interest for APPECVD (Tendero *et al* 2006). Such plasmas operate at temperatures close to room temperature with highly energetic electrons that generate active species, providing a reactive but mild medium for chemical vapor deposition. This allows a wider variety of substrate materials for deposition.

For the deposition of thin films, the dielectric barrier discharge (DBD) and atmospheric pressure plasma jet (APPJ) are the two mostly used devices to produce low temperature plasmas.

Classical plasma physics models (Reece Roth 1995) describe correctly low pressure plasmas but fail in describing high pressure non-thermal plasmas in which the collision frequency and the flow dynamics play a major role. The DBD behavior has been studied in several papers (Golubovskii *et al* 2002, Brandenburg *et al* 2005, Bogaerts *et al* 2006, Choi *et al* 2006, Massines *et al* 2008, Petrovic *et al* 2009), leading to an improved understanding of the discharge mode transition and the collision mechanisms leading to plasma species generation, but background gas flow is usually not accounted for. Operating at atmospheric pressure, the flow dynamics can, however, play a critical role. Studying the deposition of silicon dioxide by means of an APPECVD reactor, for example, the reactor performance was shown to be strongly affected by the flow dynamics. The features of the deposited layers were observed to be related to the discharge properties (Descamps *et al* 2011), but more importantly by the bulk gas flow pattern (Descamps *et al* 2013) which determines the precursor molecule residence time in the plasma region and as such plays a key role in their interaction. The experimentally observed (a)symmetric spreading of a plasma jet during its propagation to the substrate was well described by computational fluid dynamics (CFD) models and local effects, such as the Coanda effect, accurately predicted. Another example of the need for a deeper understanding of the flow dynamics for the design and scale-up of atmospheric plasma devices was given by Gaudi *et al* (2011). Using a confined helium plasma jet for thin film deposition, two flow dynamics modes were observed. A laminar mode allowed air entering the confinement tube, whereas this was prevented in a turbulent mode. The latter also resulted in a

more homogeneous plasma discharge which had a positive impact on the deposited film.

The coupled simulation of the flow dynamics, electric field and plasma chemistry is, however, challenging because of its multi-scale nature. As a result, simulations suffer from numerical stiffness and related long computation times (see e.g. Kleijn *et al* 2007). Therefore, most plasma fluid models described in the literature that focus on the description of the plasma discharge and the generated species are 1D (Golubovskii *et al* 2002, Benilov and Naidis 2003, Bogaerts *et al* 2006, Choi *et al* 2006, De Bie *et al* 2011) or even pseudo-1D (Van Gaens and Bogaerts 2013), i.e. not accounting for the bulk flow dynamics. 1D models assuming fully developed and ideal background flow were also used to study species propagation and deposition rates, but the coupling between the flow dynamics and the reactions/electric field is usually one-way, that is, the influence of the plasma discharge on the flow dynamics is usually neglected (Reece Roth 1995, Barranco *et al* 2001, Golubovskii *et al* 2002, Benilov and Naidis 2003, Foest *et al* 2003, Brandenburg *et al* 2005, Massines *et al* 2005, Bogaerts *et al* 2006, Choi *et al* 2006, Enache *et al* 2007, Petrovic *et al* 2009, De Bie *et al* 2011, Van Gaens and Bogaerts 2013). Whereas applicable for simple geometries such as two plane electrodes separated by a gap of a few millimeters, a 1D approach fails to describe accurately complex plasma jet reactors. In such reactors, specific electrode configurations generate a spatially non-uniform electric field and the flow pattern determines the distribution of the active species in the reactor and their contact with the remotely introduced chemical precursor. Few papers report on 2D plasma-fluid reactor simulations, e.g. Armaou *et al* (1999), Golubovskii *et al* (2005), Gadonna *et al* (2011), Lin *et al* (2012a, 2012b) and Punjabi *et al* (2014), the latter for an inductively coupled plasma reactor, however. Such 2D simulations typically focus on the calculation of the flow and/or electromagnetic field and assume a given species density distribution, not explicitly accounting for the crucial details of the plasma chemistry (as shown in e.g. Lozano-Parada and Zimmerman 2010). Lin *et al* (2012, 2012b) developed a 2D low-temperature, atmospheric-pressure plasma fluid model and parallel code for the simulation of helium DBDs. It allows solving the species concentrations and the electric field and accounting for the details of the plasma chemistry. Convective transport and the coupling of the latter with other phenomena were, however, neglected, so that the Navier–Stokes equations did not have to be solved. 2D simulations of an AC (RF) operated, low-pressure cylindrical showerhead electrode PECVD reactor for the deposition of amorphous silicon were presented by Armaou *et al* (1999). Both the bulk and surface reactions were accounted for, the latter assumed instantaneous. The calculation of the flow dynamics was simplified using an approximate analytical solution of the Navier–Stokes equations and a steady-state electron density profile was calculated assuming a diffusion-controlled discharge. 2D simulations of atmospheric pressure discharge that account for both the flow dynamics and chemistry are mostly reported for simple geometries. A 2D simulation of a classical CVD reactor with a complex geometry, calculating both the flow pattern in the reactor and the deposition reactions on a wafer, was reported by Cheimarios *et al* (2010). Breden *et al* (2012) developed a self-consistent, multi-species, multi-temperature 2D plasma model accounting for detailed finite-rate chemistry and photo-ionization to study the propagation of streamers in a cold, atmospheric-pressure helium jet in ambient air. In later work, Breden and Raja (2014) carried out simulations of a cold atmospheric plasma jet interacting with a dielectric surface normal to the jet, pre-computing a base fluid flow field from the Navier–Stokes equations. Xiong *et al* (2013) used a 2D plasma hydrodynamics model with radiation transport to study atmospheric-pressure plasma transfer across dielectric channels and tubes. 3D tubes were represented by 2D channels. 2D versus 3D simulations were for example compared by Hoekstra and Kushner (1998), simulating etching profiles of finite length trenches.

In previous work, the flow dynamics of an APPECVD reactor was studied by means of CFD simulations that did not account for the interaction with the electric field or the plasma chemistry (Descamps *et al* 2013). The simulations showed the crucial effect of the flow dynamics. To evaluate the interaction flow dynamics-discharge and the magnitude of the effect of the discharge on the reactor behavior, the present work addresses the modeling and efficient coupled simulation of the flow dynamics, electric field and plasma chemistry in a low-temperature, atmospheric-pressure pure nitrogen plasma. Model reduction to deal with the numerical stiffness is discussed and the proposed approach tested. 2D simulations with two different configurations are shown and the coupling between the flow dynamics, electric field and reactions and related species concentration fields discussed. In Case study I, a sharp-end plate-to-plane configuration is considered, in Case study II a specific reactor prototype for low-temperature, atmospheric-pressure plasma-enhanced chemical vapor deposition for in-line surface treatments. Operation with direct current is considered, but the proposed model and approach can be applied with alternating current as well, provided that care is taken about the calculation of the transport parameters and rate coefficients (Hagelaar and Pitchford 2005).

2. Simulation model

A model is presented for the 2D coupled simulation of the flow dynamics, electric field and plasma chemistry in low-temperature, atmospheric-pressure pure nitrogen plasma devices.

2.1. Continuity/conservation equations

The conservation equations for total mass, momentum and energy are solved along with the species continuity equations. The latter were modified to describe the effect of the electric field on the species fluxes and on the bulk flow. A Reynolds-averaged Navier–Stokes (RANS) approach is adopted. Turbulent transport is accounted for by means of a turbulent diffusivity, viscosity and conductivity. Except in the near-wall boundary layer, the standard k–ε model with standard values of the model parameters is used to model the

turbulence (Launder and Spalding 1972, Froment *et al* 2010, Wilcox 2006). Although strictly only valid for fully turbulent and developed flow without reactions (Launder and Spalding 1972), the k–ε model has been shown to be relatively accurate for free-shear layer, wall-bounded and internal flows provided that the pressure gradient is relatively small (Bardina *et al* 1997). Because of the low computation cost of the k–ε model compared to that of more advanced turbulence models and its relatively good accuracy for a wide variety of flows, it has been widely used for the simulation of industrial and environmental flows and is applied in this work. For unsteady flows, an unsteady RANS (URANS) or a computationally more costly large eddy simulation (LES) approach may be required for an accurate simulation of the turbulent mixing. The flows calculated in this work were essentially statistically stationary.

The Reynolds-averaged conservation equations for mass and momentum can be written:

$$\frac{\partial}{\partial t}(\rho_{\mathrm{g}}) + \overline{\nabla} \cdot (\rho_{\mathrm{g}} \overline{u}) = 0 \tag{1}$$

$$\frac{\partial}{\partial t}\left(\rho_{\mathrm{g}} \overline{u}\right) + \overline{\nabla} \cdot \left(\rho_{\mathrm{g}} \overline{u}\,\overline{u}\right) = -\,\overline{\nabla}\, p^{\mathrm{eff}} + \overline{\nabla} \cdot \overline{\overline{\tau}}_{\mathrm{g}}^{\mathrm{eff}} + \rho_{\mathrm{g}} \overline{g} + \rho_{\mathrm{el}} \overline{E} \tag{2}$$

The term $\rho_{\mathrm{el}}\overline{E}$ accounts for momentum transfer between electrically driven species and the bulk gas.

The process gas temperature is of primary importance in applications where the substrate and/or the deposited layer are thermo-sensitive. Excessive temperatures might also damage the reactor. An accurate calculation of the temperature distribution in the reactor allows selecting the proper construction materials and optimizing the reactor design and operating conditions. The heat is assumed to be mainly produced by Joule heating in the electrodes as a result of the carried current. A heat source is therefore imposed at the electrodes. The heat effect of plasma species collisions and the heat of reaction, especially for the fast reactions, are considered negligible because of the low degree of ionization. The energy conservation equation is then given by:

$$\frac{\partial}{\partial t}(\rho_{\mathrm{g}} H) + \overline{\nabla} \cdot (\rho_{\mathrm{g}} H \overline{u}) = -\,\overline{\nabla} \cdot (p^{\mathrm{eff}}\, \overline{u}) + \overline{\nabla} \cdot (\lambda_{\mathrm{g}}^{\mathrm{eff}}\, \overline{\nabla}\, T_{\mathrm{g}}) + \rho_{\mathrm{g}} \overline{u} \cdot \overline{g} + \overline{\nabla} \cdot \left(\overline{u} \cdot \overline{\overline{\tau}}_{\mathrm{g}}^{\mathrm{eff}}\right) \tag{3}$$

Note that the above mentioned assumptions on the heat source terms are not valid in many low-temperature atmospheric-pressure plasmas, in which heating by a few to a few hundreds of degrees is not uncommon. It has to be verified for each specific case if neglecting plasma heating is justified.

The considered plasma contains various species among which electrons, positive ionic species, excited states of neutral background gas, and dissociated atoms as the main reactive species. For all of these species, the continuity equation can be formally written as:

$$\frac{\partial}{\partial t}(\rho_{\mathrm{g}} x_j) + \overline{\nabla} \cdot \overline{\Gamma}_j = S_j \tag{4}$$

The description of the species flux $\overline{\Gamma}_j$ depends on the considered species. For electrically neutral species n, the flux $\overline{\Gamma}_n$ includes convection and diffusion:

$$\overline{\Gamma}_n = \rho_g x_n \overline{u} - \rho_{\mathrm{g}} D_n^{\mathrm{eff}}\, \overline{\nabla}\, x_n \tag{5}$$

Electrically charged species—ionic species i and electrons e—are assumed to be essentially driven by the electric field (Huxley and Crompton 1974) and the influence of bulk flow is neglected. The gas flow velocity is expected to be several orders of magnitude lower than the drift velocity. The influence of the electric field is accounted for by a drift term, so that the ion and electron fluxes can be written:

$$\overline{\Gamma}_{\mathrm{i}} = \frac{q_{\mathrm{i}}}{|q_{\mathrm{i}}|} \mu_{\mathrm{el,i}} \overline{E}\, \rho_{\mathrm{g}} x_{\mathrm{i}} - \rho_{\mathrm{g}} D_{\mathrm{i}}\, \overline{\nabla}\, x_{\mathrm{i}} \tag{6}$$

$$\overline{\Gamma}_{\mathrm{e}} = -\mu_{\mathrm{el,e}} \overline{E}\, \rho_{\mathrm{g}} x_{\mathrm{e}} - \rho_{\mathrm{g}} D_{\mathrm{e}}\, \overline{\nabla}\, x_{\mathrm{e}} \tag{7}$$

In (6) and (7), $\mu_{\mathrm{el,i}}$ and $\mu_{\mathrm{el,e}}$ are the electrical mobility of ions and electrons respectively, D_{i} and D_{e} the diffusion coefficient of ionic species and electrons. Their calculation is discussed hereafter.

The term S_j in the species continuity equations (4) is the source term related to the generation and consumption of species j by chemical reactions. It has the general form:

$$S_j = M_j \sum_k \alpha_{jk} R_k \tag{8}$$

where M_j is the molar mass of species j, α_{jk} is the stoichiometric coefficient of species j in reaction k and R_k is the rate of reaction k. For ionic species, S_{i} accounts for direct ionization, ion–electron recombination and charge transfer between ions. For electrons, S_{e} accounts for the electron production through neutral-electron and excited species collisions (Penning ionization) and electron recombination with positive ions. Note that because the total mass conservation is also used, only $(N-1)$ species continuity equations must be solved in a system containing N species. The unsolved equation is chosen to be that of the background process gas.

The chemical efficiency of low temperature plasmas is due to the existence of high energy electrons that are able to interact with heavy species such as neutral gas species and ions that have a temperature close to room temperature. Because of their high energy and the low ionization degree, electrons are not at thermodynamic equilibrium with the surrounding gas and obey their own energy distribution function. The latter allows relating the electron mean energy ϵ_{e} to the electronic temperature:

$$\epsilon_{\mathrm{e}} = \frac{3}{2} k_{\mathrm{B}} T_{\mathrm{e}} \tag{9}$$

Electrical transport properties depend on the electron mean energy. The latter also strongly affects the rate of plasma reactions. The electron energy distribution function and mean energy can be calculated from collision cross section data available in the literature (Itikawa 2006) and solving the Boltzmann equation (Hagelaar and Pitchford 2005). The latter is computationally demanding. As explained in

Table 1. Reaction mechanism and rate coefficients for pure nitrogen plasma. References: (a) Kossyi *et al* (1992); (b) Van Gaens and Bogaerts (2013).

	Reaction	Rate coefficient	Units	Reference
1	$N_2 + e \rightarrow N_2(A) + e$	$2.4 \times 10^{12-140/\theta}$	$(m^3\,kmol^{-1} \cdot s^{-1})$	(a)
2	$N_2 + e \rightarrow N_2(a) + e$	$1.9 \times 10^{12-174/\theta}$	$(m^3\,kmol^{-1} \cdot s^{-1})$	(a)
3	$N_2 + e \rightarrow N_2(B) + e$	$3.8 \times 10^{12-148/\theta}$	$(m^3\,kmol^{-1} \cdot s^{-1})$	(a)
4	$N_2 + e \rightarrow N_2(C) + e$	$3.8 \times 10^{12-211/\theta}$	$(m^3\,kmol^{-1} \cdot s^{-1})$	(a)
5	$N_2 + e \rightarrow 2N + e$	$3.8 \times 10^{10-350/\theta}$	$(m^3\,kmol^{-1} \cdot s^{-1})$	(a)
6	$N_2 + e \rightarrow N_2^+ + 2e$	$3.0 \times 10^{12-365/\theta}$	$(m^3\,kmol^{-1} \cdot s^{-1})$	(a)
7	$N_2(A) + N_2(a) \rightarrow N_4^+ + e$	5.4×10^9	$(m^3\,kmol^{-1} \cdot s^{-1})$	(b)
8	$2N_2(a) \rightarrow N_4^+ + e$	6.0×10^9	$(m^3\,kmol^{-1} \cdot s^{-1})$	(b)
9	$2N \rightarrow N_2^+ + e$	6.0×10^8	$(m^3\,kmol^{-1} \cdot s^{-1})$	(a)
10	$N_4^+ + e \rightarrow 2N_2$	$1.9 \times 10^{14}\sqrt{1/T_e}$	$(m^3\,kmol^{-1} \cdot s^{-1})$	(b)
11	$N_2^+ + e \rightarrow 2N$	$1.5 \times 10^9\sqrt{1/T_e}$	$(m^3\,kmol^{-1} \cdot s^{-1})$	(b)
12	$2N + N_2 \rightarrow 2N_2$	$5.0 \times 10^{13}\exp(500/T_g)$	$(m^6\,kmol^{-2} \cdot s^{-1})$	(b)
13	$N_2(A) + N_2 \rightarrow 2N_2$	2.2×10^5	$(m^3\,kmol^{-1} \cdot s^{-1})$	(b)
14	$N_2(A) + N \rightarrow N_2 + N$	1.2×10^{10}	$(m^3\,kmol^{-1} \cdot s^{-1})$	(b)
15	$N_2(B) + N_2 \rightarrow N_2(A) + N_2$	3.0×10^{10}	$(m^3\,kmol^{-1} \cdot s^{-1})$	(a)
16	$N_2(B) \rightarrow N_2(A)$	1.5×10^5	(1 /s)	(a)
17	$N_2(a) + N_2 \rightarrow N_2(B) + N_2$	1.2×10^8	$(m^3\,kmol^{-1} \cdot s^{-1})$	(a)
18	$N_2(C) \rightarrow N_2(B)$	3.0×10^7	(1 /s)	(a)
19	$N_2(C) + N_2 \rightarrow N_2(a) + N_2$	6×10^9	$(m^3\,kmol^{-1} \cdot s^{-1})$	(a)
20	$N_2^+ + 2N_2 \rightarrow N_4^+ + N_2$	1.8×10^{13}	$(m^6\,kmol^{-2} \cdot s^{-1})$	(b)
21	$N_4^+ + N_2 \rightarrow 2N_2 + N_2^+$	$1.5 \times 10^6(10^{0.0036(T_g-300)})$	$(m^3\,kmol^{-1} \cdot s^{-1})$	(a)

Hagelaar and Pitchford (2005), a common approach to avoid excessive calculation time is to solve an approximation of the Boltzmann equation for a number of values of the reduced electric field θ and to generate tables of the resulting transport properties and rate coefficients versus the reduced electric field. For the CFD model/calculation, the tables can then be used to find values for the local transport properties and rate coefficients by interpolation. If an electron energy equation is not solved, a similar strategy can be used for the estimation of the mean electron energy. This is the approach adopted in this work. Solutions provided by the Boltzmann equation solver BOLSIG+ (Chen and Davidson 2002) were used and linearly interpolated to derive correlations for the mean electron energy and the electrical mobility $\mu_{el,e}$ and diffusivity D_e of the electrons (Hagelaar and Pitchford 2005) as a function of the calculated reduced electric field θ. These correlations were used in the CFD code. The transport coefficients for ionic and neutral species were taken from the literature (Ionic data: Tables 2 and 4: Ellis *et al* 1978, Viehland and Mason 1995).

2.2. Plasma reaction mechanism and kinetics

The coupling of chemical reactions with CFD is computationally costly, on the one hand because of the number of species continuity equations to be solved, on the other hand because of the Arrhenius dependence of reaction rates on the temperature. With complex reaction mechanisms, reduced or lumped reaction schemes (e.g. Baudrez *et al* 2010) are typically used. The set of 21 reactions included in the model in this work is given in table 1 and adopted from the literature. The process gas is assumed to be pure nitrogen. A total of 9 species are considered including neutral and charged species. The neutral species are the background gas N_2, the dissociated N atom and 4 types of electronically excited neutral nitrogen plasma species: $N_2(A^3\Sigma_u^+)$, $N_2(B^3\Pi_g)$, $N_2(a'\,^1\Sigma_u^-)$ and $N_2(C^3\Pi_g)$. For practical reasons, the shortened notations $N_2(A)$, $N_2(B)$, $N_2(a)$ and $N_2(C)$ are used. Among those species, it is possible to distinguish the long-lived metastable $N_2(A)$ and $N_2(a)$ species which are of primary importance in understanding a low-temperature discharge (Brandenburg *et al* 2005) and precursor decomposition. $N_2(A)$ is reported to be the main species interacting with a chemical precursor in remote plasma devices (Enache *et al* 2007). $N_2(B)$ and $N_2(C)$ are short-lived species mostly recombining though radiative and collisional processes (reactions 16 and 18 in table 1) (Bak *et al* 2011). The rotational and vibrational states of nitrogen molecules are not included in the present model, their effect on chemical precursor decomposition and on the discharge features being small compared to that of the electronic state. In addition to electrons, 2 ionic species are considered in the present model: N_2^+, and N_4^+. Electron attachment to nitrogen is unlikely at low ionization degree (Brandenburg *et al* 2005). Negative ionic species are therefore not included. Very short-lived excited states or ionic species present in negligible concentrations were also not taken into account.

The 21 considered reactions include direct excitation, ionization and dissociation of background nitrogen, relaxation of excited states through radiative processes and collisions

with neutrals, recombination of electrons and ions and charge transfer. Other sources of ionization/electrons, such as photo/UV-ionization are not included in the model. This may be problematic, especially when electrons are lost fast, such as at a high potential between the electrodes. Most of the reactions considered involve background N_2 gas whose concentration remains practically constant and several orders of magnitude higher than that of any plasma species, so that most reactions are pseudo-first order. The rate coefficients were taken from the literature and are also shown in table 1. Given that most of the reactions are pseudo-first order, the effect of turbulent mixing on the reaction rates is neglected.

2.3. Electric field

A complete and accurate description of the electric field distribution theoretically requires solving the Maxwell equations for electromagnetism. For DC operation or AC operation with frequencies of typically up to ±50 kHz, the typical reactor length scale is, however, small compared to the electromagnetic wavelength induced by electric field variation. A similar conclusion can be drawn when comparing the characteristic time scale of the modeled phenomena and the electromagnetic wave propagation velocity. The resulting quasi-steady state behavior allows the use of a pseudo-electrostatic model, where the potential Φ is given by the Poisson equation:

$$\overline{\nabla} \cdot (\epsilon_0 \overline{\nabla} \Phi) = -\left(\sum_{\mathrm{i}} q_{\mathrm{i}} n_{\mathrm{i}} - q_{\mathrm{e}} n_{\mathrm{e}} \right) \tag{10}$$

with ϵ_0 the vacuum dielectric constant (Lin *et al* 2012a, 2012b). It is assumed that the plasma does not affect the medium permittivity. In (10), q_{i} and q_{e} are respectively the charge of ionic species i and the electronic charge and n_{i} and n_{e} are the ionic and electron density. The electric field is calculated as the gradient of the electrical potential:

$$\overline{E} = -\overline{\nabla}\Phi \tag{11}$$

2.4. Boundary conditions

Interactions between charged species and an electrode surface are of primary importance in sustaining the discharge in low temperature plasmas (Golubovskii *et al* 2002). In near-dielectric regions, charged species accumulate, resulting in the formation of a so-called plasma sheath. This sheath shields the bulk plasma from the externally applied voltage. The sheath thickness can be estimated from the Debye equation. At atmospheric pressure it is often of the order of a few micrometers. The properties of plasma sheaths are used to define boundary conditions at dielectric electrodes. Electronically excited states and dissociated atoms N are instantaneously quenched when reaching an electrode surface. Golubovskii *et al* (2002) considered different interactions to model the influence of dielectric electrode surface interactions on atmospheric-pressure low-temperature discharges. The metastable species $N_2(A)$ is believed to be responsible for secondary electron emissions (Brandenburg *et al* 2005, Enache *et al* 2007).

Table 2. Interactions of charged species with a dielectric wall. References: (a) Brandenburg *et al* (2005); (b) Golubovskii *et al* (2002); (c) Lin *et al* (2012a, 2012b).

	Reaction	Rate expression (1/(m² · s))	Reference
1	Secondary electron emission by photon absorption	γ_{p}	(a)
2	Secondary electron emission by collisions of metastable species	$\gamma_{\mathrm{m}} D_{\mathrm{A}} \nabla n_{N_2(A)}$	(a)
3	Secondary electron emission by interactions with ions	$\gamma u_{\mathrm{i}} n_{\mathrm{i}}$	(b)
4	Electron transport to the surface	$u_{\mathrm{e}} n_{\mathrm{e}}$	(c)
5	Ion transport to the surface	$u_{\mathrm{i}} n_{\mathrm{i}}$	(c)

Secondary electron emissions also result from collisions of ions with the wall and photon absorption. The total secondary electron emission current from a dielectric electrode is, hence, given by:

$$\overline{j_{\mathrm{s}}} = \gamma \sum_{\mathrm{i}} \overline{u}_{\mathrm{i}} n_{\mathrm{i}} + \gamma_{\mathrm{m}} D_{\mathrm{A}} \overline{\nabla} n_{N_2(A)} + \overline{\gamma}_{\mathrm{p}} \tag{12}$$

γ, γ_{m} and $\overline{\gamma}_{\mathrm{p}}$ are the secondary electron emission coefficients for ion-surface interactions, metastable species collisions with the wall and photon emissions, respectively. For $\overline{\gamma}_{\mathrm{p}}$, a value of $1.578 \cdot 10^{-14}$ (1/(m² · s)) was imposed. This value was obtained by integrating a general expression for photon emission (Brandenburg *et al* 2005) with a constant averaged metastable species density. Higher values for the secondary electron emission coefficients are often used to sustain a discharge and compensate for an electron deficit when electrons are consumed fast at an electrode by recombination and certain mechanisms of ionization, such as photo-ionization, are not accounted for in the model (Zakari *et al* 2015). The boundary conditions to account for surface interactions can then be written

$$\overline{\Gamma_{\mathrm{e}}} = -\alpha_{\mathrm{r}} \rho_{\mathrm{g}} x_{\mathrm{e}} \rho_{\mathrm{g}} x_{\mathrm{i}} \overline{n} + m_{\mathrm{e}} \overline{j_{\mathrm{s}}} \tag{13}$$

$$\overline{\Gamma_i} = -\alpha_{\mathrm{r}} \rho_{\mathrm{g}} x_{\mathrm{e}} \rho_{\mathrm{g}} x_{\mathrm{i}} \overline{n}, \tag{14}$$

for electrons and ions respectively. The first term on the right hand side of (13) and (14) represents consumption of respectively electrons and ions by recombination at the wall. Charged species heading towards a dielectric electrode will accumulate in the near-wall region and be consumed by surface recombination (Lozano-Parada and Zimmerman 2010). This accumulation will create strong gradients in the electric field in the near-dielectric wall region. This makes the accurate calculation of the electric field extremely challenging. The electric field variation in the discharge core is in contrast typically rather smooth. The interactions with a dielectric wall that are considered in this work are summarized in table 2. The electric field inside the dielectric is assumed to vary in the direction perpendicular to the surface only. A relation between the imposed electrode voltage, the surface charge and the voltage difference between the gas and the electrode can be derived from this 1D assumption. This approach is strictly only valid if the dielectric thickness is small compared to the

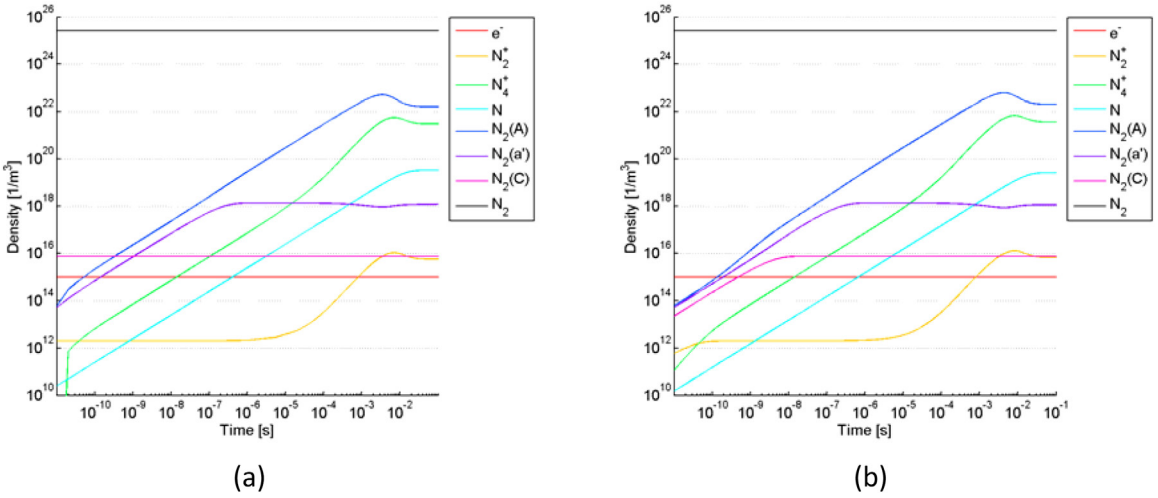

Figure 1. Evolution in time of the species concentrations in a pure nitrogen plasma after applying a constant electric field of 3.5×10^6 V m^{-1}. 0D simulations (batch) (a) without kinetic model reduction and (b) applying the quasi-steady state (QSS) approximation on $N_2(B)$, $N_2(C)$ and N_2^+, allowing increasing the time step with a factor 10^4.

width of the discharge region so that the voltage drop within the dielectric is negligible.

Charges reaching a grounded metallic electrode surface are assumed to be immediately transported outside the discharge region by electrical conduction. At metallic non-electrode walls, the boundary condition for the electrical voltage follows from a zero-electric field assumption in the direction normal to the wall. Excited species $N_2(A)$, $N_2(B)$, $N_2(C)$ and $N_2(a')$ are assumed to relax instantaneously upon collision with a wall and their density n (1/m^3) is imposed to be zero at the walls and, hence, at the electrodes.

In Case study II, heat transfer through the reactor walls is calculated from:

$$\overline{q}_w = h_g(T_g - T_{wg})\overline{n} = \lambda_w(T_{wg} - T_{we})\overline{n} = h_e(T_{we} - T_\infty)\overline{n} \tag{15}$$

with h_g the coefficient of heat transfer between the inner wall and the process gas calculated by means of the correlation of Jayatilleke (1969) and h_e the coefficient of heat transfer between the external wall and the surroundings for which a typical value of 25 (W m^{-2}.K^{-1}) was used.

2.5. Kinetic model reduction

The rate coefficients of some of the reactions considered reach extremely high values, leading to numerical stiffness and related convergence problems and long computation times. For fast reacting and, hence, short-lived species, the quasi-steady state (QSS) approximation can be applied to reduce the computational complexity. Transport by convection, diffusion and drift can then be neglected, their time scale being large compared to that of the fast reactions, and the continuity equations for short-lived species are reduced to:

$$\frac{\partial \rho_g x_j}{\partial t} = M_j \sum_k \alpha_{jk} R_k = 0 \tag{16}$$

Hence, for the short-lived species, the solution of a partial differential equation is no longer required. Algebraic equation (16) can be directly used to calculate the species mass fraction. The quasi-steady state approximation was applied for species $N_2(B)$ and $N_2(C)$ as well as for the ionic species N_2^+. The steady state density of N_2^+ is relatively low and the total positive charge will be mostly carried by N_4^+. The species N_2^+ can, however, not be neglected because they are a necessary intermediate for the formation of ionic species by electron–nitrogen collisions. The steady state density of N_2^+ being rapidly reached (within about 10^{-8} s at atmospheric pressure, see also Brandenburg *et al* 2005) because of the fast charge transfer reaction between N_2^+ and N_4^+ allows applying the QSS approximation. From transient 2D test simulations with a pulse release at the anode, the transport time of the N_2^+ and N_4^+ ions to the cathode was found to be of the order of 0.1 ms in a 10^7 V m^{-1} electric field (10 kV imposed potential)—about one order of magnitude larger than that of electrons, so that the time scale of reaction can be considered small compared to that of transport. Other excited species $N_2(A)$ and $N_2(a)$ are not quenched as efficiently by collision with the ground state or through radiative processes. The remaining computationally challenging reactions were identified to be the Penning ionization reactions 7 and 8 (table 1), transforming electronically excited states to ionic species following collision.

The validity of the quasi-steady state approximation was verified through transient 0D simulations with direct current and an electric field ranging from 10^6 (V m^{-1}) to 10^7 (V m^{-1}). Figure 1 shows the evolution of the molar concentration of various species with time obtained without and with the quasi-steady state approximation in a constant electric field of 3.5×10^6 (V m^{-1}). No significant differences are observed at the typical transport time scales (10^{-6} s) or larger. Figure 1 shows that the steady state plasma composition is reached within about 10^{-2} s and shows the QSS approximation cannot be applied to all species. When the voltage is turned off, the evolution of the species concentrations confirms that in the plasma reactors studied, only long-lived species (especially metastable $N_2(A)$ and $N_2(a)$) can be expected at a certain

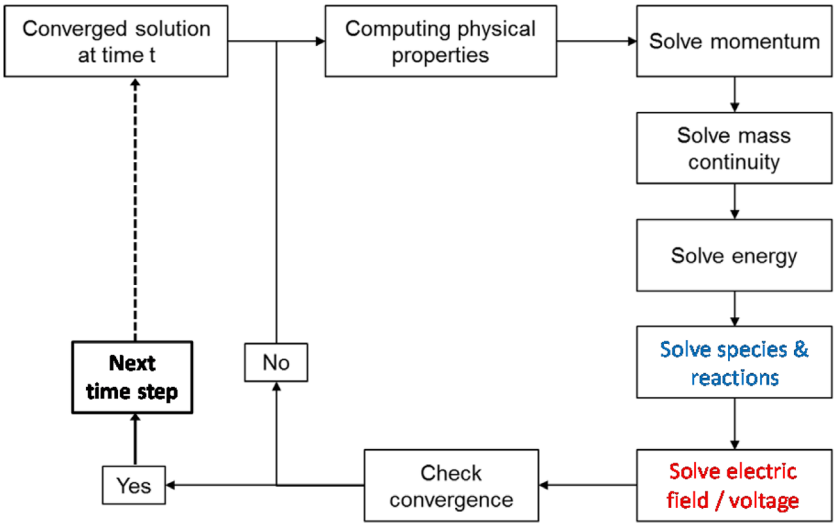

Figure 2. Solution algorithm.

distance from the discharge region. Other species will have mostly relaxed or recombined near the discharge region. The stationary concentrations of the different species in the 0D simulations differ by several orders of magnitude. N_4^+ is the main observed ionic species and mostly produced through the fast conversion of N_2^+ (reaction 21, table 1). A typical ionization degree of 1.15×10^{-4} in the 3.5×10^6 (V m^{-1}) electric field is reached. The metastable $N_2(A)$ nitrogen state is the only species whose density is comparable, with a relative density of 8×10^{-4} compared to the background nitrogen. Its relaxation time is extremely long compared to that of other excited states. It is expected to be practically the only active species found outside the discharge region and responsible for the decomposition of a chemical precursor, if injected remotely.

3. Solution algorithm

Simulations were carried out using the unstructured finite volume CFD code Fluent 6.3.26 (Ansys). Electric field-related terms, such as appearing in equatios (2), (6) and(7), cannot be integrated in the standard conservation and species continuity equations defined in Fluent. User-defined scalar transport equations (UDS) were therefore used. For specific transport properties and the reaction source terms, user-defined functions (UDF) were defined. The solution algorithm is schematically shown in figure 2. The flow field, the species concentrations and reactions, and the electric field are sequentially solved in an iterative loop. For the flow field and species concentration calculation, time-stepping was applied. The SIMPLE algorithm was used for optimal pressure-velocity coupling. Typically, the flow field is first calculated in the absence of an electric field and reactions. Next, the plasma is ignited and the flow dynamics, electric field and plasma chemistry solved in a coupled way. A semi-implicit scheme and second-order discretization in time and space were used to improve the accuracy of the solution. The estimated relative error on the computed values of the species concentrations reaches fast extremely low values. Hagelaar and Kroesen (2000) proposed a method for speeding up CFD simulations of gas discharges, but an implicit treatment of the electron energy source term is essential. With a sequential solution of the flow, species concentration and electric fields, the solution of each equation can eventually be done in a (semi-)implicit manner, for example with an iterative scheme as proposed in Kushner (2009).

The time scales of the modeled phenomena impose the use of extremely small time steps. The reactor mean residence time is of the order of 10^{-1} s, whereas the time scale of the electrical transport of ions and electrons is of the order of 10^{-6} to 10^{-5} s and the excitation and ionization reactions take place within 10^{-10} to 10^{-9} s. Together with the use of the Poisson equation (10), the quasi-steady state hypothesis assumed for the short-lived species and N_2^+ ions helps reducing the numerical stiffness. A sharp transition from convergence to divergence is observed for a time-step of around 10^{-8} s. In the early stage of a simulation, time steps of 10^{-10} s are used, despite the use of the quasi-steady state approximation for the short-lived species, but the time step can be slowly increased to 10^{-7} s while reaching the steady state solution. Moreover, modeling the near-wall and near-electrode plasma behavior requires capturing the steep voltage and concentration gradients in their vicinity. This implies the use of mesh cells drastically smaller in these regions than in the bulk gas region. The thickness of the near-electrode region where the species concentration and electric field gradients are strong is indeed of the order of a few microns only. Near the electrodes, mesh cells as small as 0.01 μm were used. The mesh size in the bulk gas region varied between 0.01 and 0.1 mm.

4. Case study I

Discharge in a sharp-end plate-to-plane configuration was simulated in 2D and starting from a zero flow field. The geometry is shown in figure 3. The top and sides of the domain are essentially open and no inflow of gas was imposed, but atmospheric pressure. The distance between the electrodes

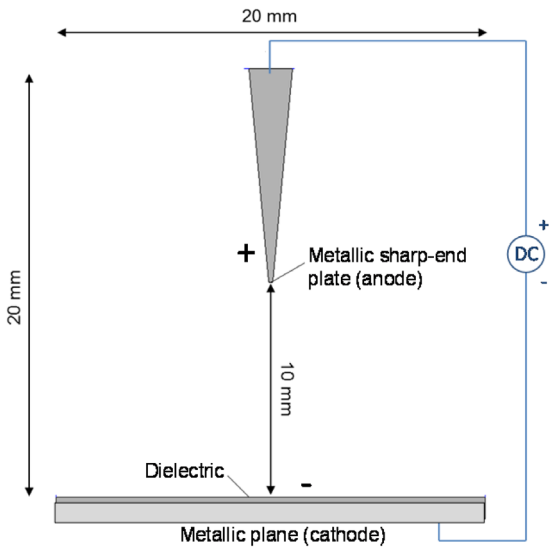

Figure 3. Case study I: sharp-end plate-to-plane configuration with an anode with a 100 μm curvature radius head.

was 10 mm. The sharp electrode tip (anode) was considered to be made of perfectly conducting metal, the plane electrode (cathode) to be covered with a thin dielectric layer. The anode had a 1 mm wide base, whereas the curvature radius of the tip head was 100 μm. The boundary conditions imposed at the electrodes were described in section 2.4. A constant potential difference of 5 kV was applied between the two electrodes. Under such conditions, a corona discharge type behavior can be expected (Tendero *et al* 2006). The required mesh size is mostly determined by the gradients in the electric field and 250 thousand mesh cells were used with mesh cells of 0.01 μm in the near-electrode region, as explained in the previous section. Details on the mesh can be found in Lorant (2013). The electric field is mostly localized near the anode tip, with values of the electric field dropping to less than half the maximum value at a distance of about 100 μm from the tip. The region where the nitrogen breakdown value (comprised between $3 \cdot 10^6$ and $6 \cdot 10^6$ V m^{-1}—Radmilovic *et al* 2014) is overcome is located in a $\pm$300 μm radius around the tip, region where plasma generation is expected to be strongly concentrated.

The discharge voltage, gas velocity, electron density and typical species concentration profiles are shown in figure 4. The electron density only reaches significant values in the near anode region, as expected in a corona discharge. Figure 4(c) therefore focuses on the electrode tip head. Ionic species produced in this region are extracted from the discharge zone by the electric field and move towards the plate cathode. As a result, the corona environment is globally positively charged. The discharge voltages are rather small compared to the applied potential difference.

The bulk flow generated by the corona discharge is not negligible and driven by the ionic wind. Velocities of 1–5 m s^{-1} are observed in between the electrodes and recirculation patterns develop in the flow domain. Moreau *et al* (2004) found a maximum gas velocity reachable by a positive DC corona of about 10 m s^{-1}. Although direct comparison is not possible, velocities of the same order of magnitude are reported by Jyaraman and Shyy (2008) (Helium discharge in 10 kHz alternating field) and Martins (2013) (different discharge conditions and ion density). Three typical species concentration profiles are shown, for respectively positively charged ions N_4^+(figure 4(d)), long-lived neutral species $N_2(A)$ (figure 4(e)) and short-lived neutral species $N_2(C)$ (figure 4(f)). The long-lived neutral species are seen to spread in the domain between the electrodes as a result of the recirculation introduced by the discharge. This is not the case for the short-lived neutral species which remains concentrated near the tip head. The positively charged ions cannot follow the recirculation flow pattern and are deflected towards the plate cathode. Note the much lower concentration of $N_2(C)$ and N_4^+ species than that of the $N_2(A)$ species (log scale). More detailed species and electron concentration profiles in between the electrodes are given in figure 5. As expected, in the corona discharge at 5 kV the electron density in the bulk gas is negligible. The electrons are concentrated close to the surface of the curved electrode, a region of high potential gradient resulting in highly energetic electrons. The ionization degree is of the order of 10^{-9}.

Both Penning ionization and secondary emission are important to sustain the discharge. When not accounting for secondary emission in the simulation ($\gamma = \gamma_m = \overline{\gamma_p} = 0$), the plasma is first ignited due to the initial very low electron density, but extinguished rapidly, that is, within of the order of 10^{-5} s, while the initially produced ions drift towards the ground electrode. When increasing the potential between the two electrodes to 10 kV, a discharge could also not be sustained. The higher voltage leads to a faster loss of electrons. Not accounting for all mechanisms of ionization, such as photo-ionization, and related sources of electrons in the model leads to an electron deficit. A similar problem was noticed by other groups and compensated for by including artificial electron sources, e.g. increasing the coefficients of secondary electron emission (Zakari *et al* 2015).

5. Case study II

A prototype of a low-temperature, atmospheric-pressure plasma-enhanced chemical vapor deposition (APPECVD) reactor was simulated in 2D imposing a 5 kV potential between the electrodes and using the previously presented model. The reactor scheme and dimensions, a figure of the applied voltage, and pictures of a similar pilot scale reactor (produced by Plasmatreat) are shown in figure 6. The reactor contains four wire electrodes, two connected to the voltage source and two grounded, all covered with a thin layer of dielectric material. A 1.5 mm gap separates anode and cathode. This distance between the electrodes can be tailored on the actual prototype but is kept constant in the simulation presented. The process gas enters the reactor chamber at 0.25 m s^{-1} through two 3 mm side inlets, while the gas carrying the chemical deposition precursor is injected at 4.5 m s^{-1} from the top through a 0.5 mm channel. All gases are fed at ambient temperature. The reactor exit is positioned 1 mm above the substrate surface. The reactors walls are made of polymer and graphite electrodes are

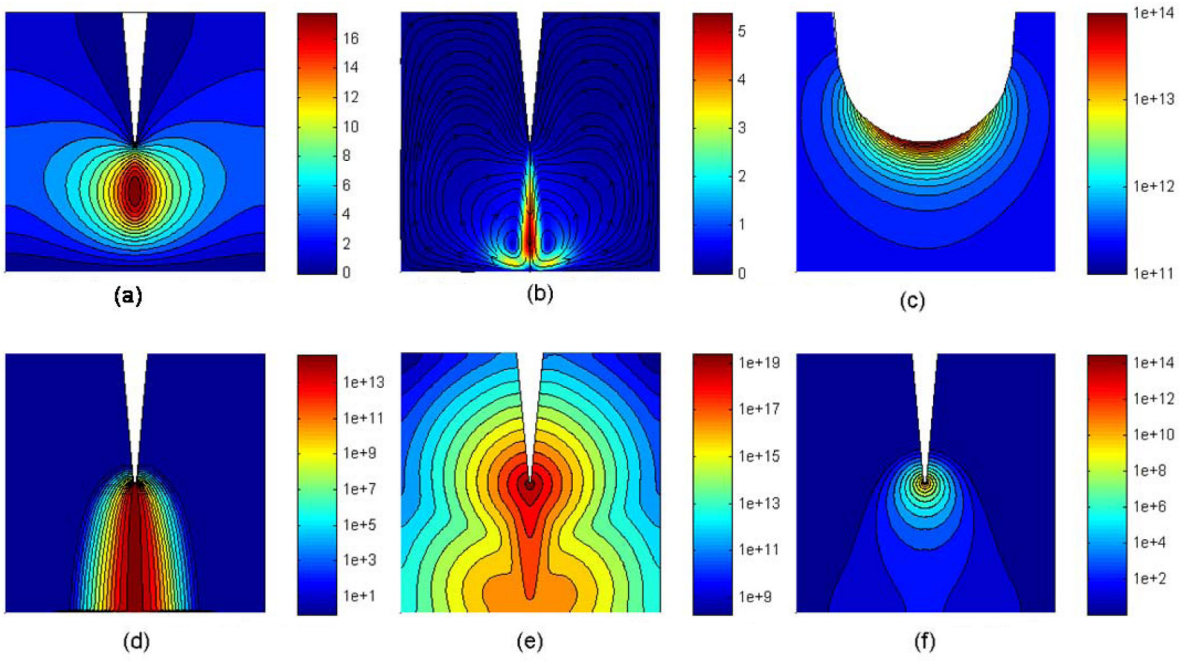

Figure 4. Case study I: 2D simulation of a sharp-end plate-to-plane configuration (figure 3) applying a 5 kV potential between the electrodes. Steady state profiles of the (a) discharge voltage (V); (b) gas velocity (m s^{-1}); (c) electron density (1/m^3) (focus on the anode tip head); (d) N_4^+ density (1/m^3); (e) $N_2(A)$ density (1/m^3); (f) $N_2(C)$ density (1/m^3).

used. Atmospheric pressure is imposed at the reactor outlet. To account for Joule heating of the electrodes, the electrode surface temperatures were experimentally measured using an IR camera and imposed in the simulations to be 250 °C and uniform. Details on the boundary conditions at the electrodes were given in section 2.4. Heat transfer through the reactor walls is calculated through (15).

Figure 7 shows the influence of the electric field and plasma reactions on the flow field. Symmetry breaking is observed both prior and after ignition. The flow of precursor carrying gas attaches to one of the two electrodes, creating recirculation in the upper part of the reactor. No oscillations in the flow pattern are observed. Almost immediately after ignition (picture after 1 μs shown), high velocities occur locally. Vortices form in the regions between the two electrodes. These vortices remain after the steady state solution is reached (figures 7(c) and (d)). With gas fed through different reactor inlets, the flow is mainly pressure driven and the influence of the plasma/ionic wind on the flow pattern is overall relatively small. This shows the fluid dynamics has a major influence on the performance of the studied APPECVD reactor. The symmetry breaking in the flow pattern may lead to precursor penetrating the discharge region, leading to formation of a powder that will be deposited on the substrate instead of a uniform thin film (Descamps *et al* 2011).

Figure 8 shows profiles of the steady state discharge voltage, gas phase temperature, electron density and N_4^+, $N_2(A)$ and $N_2(C)$ species concentrations. The field intensity is concentrated in the two regions between anodes and cathodes and the field lines are rather uniform in these regions. The nitrogen breakdown voltage being $3.1 \cdot 10^6$ V m^{-1}, the discharge is expected to be located in this region. Short-lived neutral species $N_2(C)$ are conveyed to a certain extent into

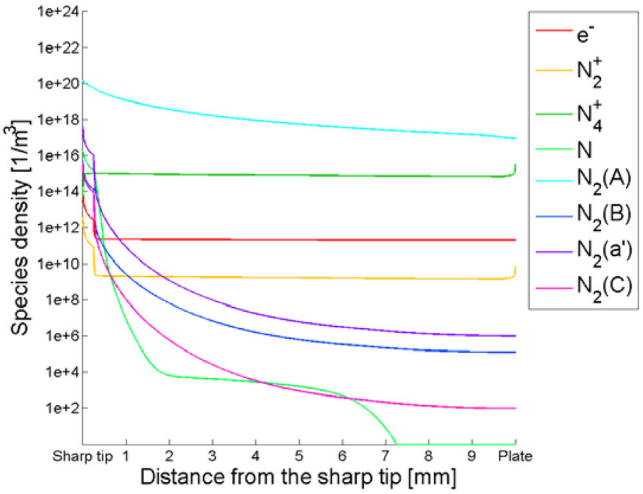

Figure 5. Case study I (figure 3). Steady state species density profiles (1/m^3) as a function of the distance from the tip when applying 5 kV potential difference between the electrodes.

the central reactor corridor, whereas the N_4^+ ions are captured more strongly in the region between the electrodes. The long-lived neutral species $N_2(A)$ are seen to spread in the reactor as a result of the up flow in between the electrodes and the reactor walls and recirculation in the reactor. Significant concentrations of $N_2(A)$ are found in the upper part of the reactor and in the central corridor. Long-lived $N_2(A)$ and $N_2(a)$ (not shown) are the only species that reach the substrate surface where their concentration is relatively uniform. They are believed to be the only species interacting with the chemical deposition precursor. The recirculation in the reactor is also clearly visible in the temperature profile shown in figure 8(b). Significant temperature variations are observed in the reactor

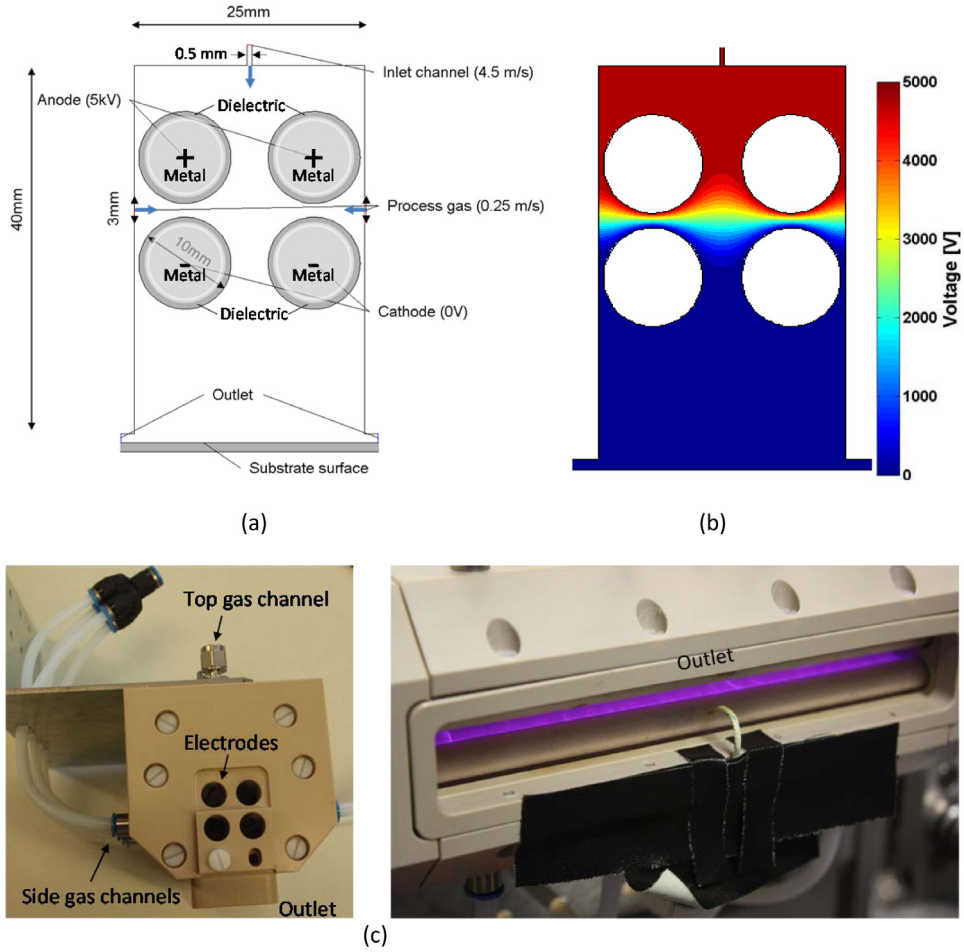

Figure 6. Case study II: reactor for in-line low-temperature, atmospheric-pressure plasma-enhanced chemical vapor deposition. (a) Reactor scheme; (b) applied voltage (V); (c) pictures of a pilot scale reactor (produced by Plasmatreat).

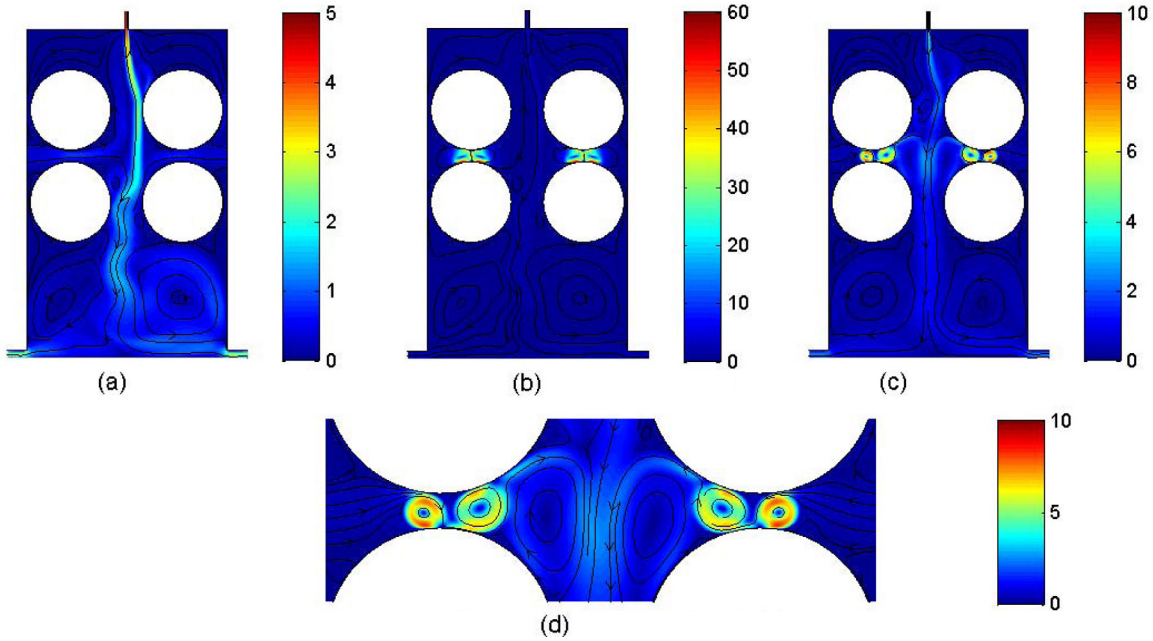

Figure 7. Case study II: reactor for in-line low-temperature, atmospheric-pressure plasma-enhanced chemical vapor deposition (figure 6). Evolution of the flow field after plasma ignition (colored by the velocity magnitude in m s^{-1}): (a) prior to ignition; (b) 1 μs after ignition; (c) after reaching the steady state; (d) focusing on the region between the electrodes after reaching the steady state.

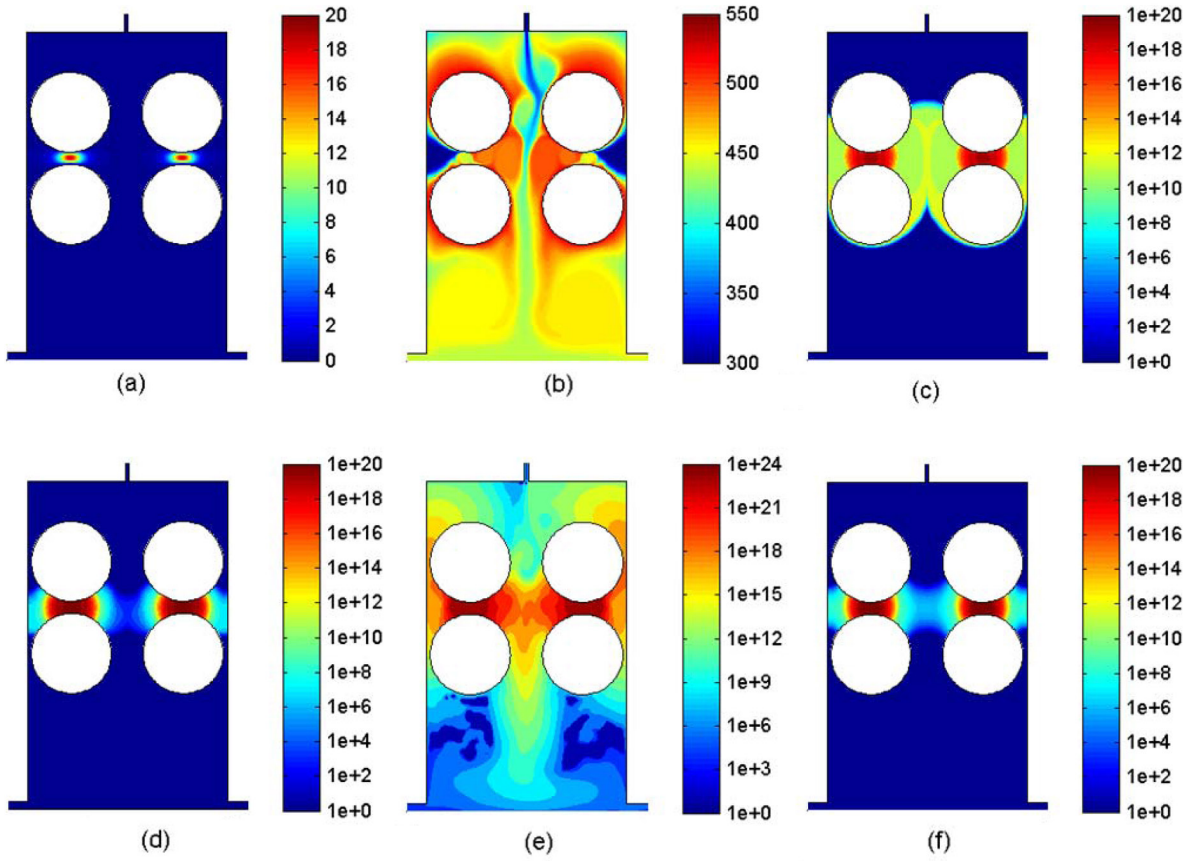

Figure 8. Case study II: reactor for in-line low-temperature, atmospheric-pressure plasma-enhanced chemical vapor deposition (figure 6). Steady state profiles of the (a) discharge voltage (V); (b) temperature (K); (c) electron density (1/m^3); (d) N_4^+ density (1/m^3); (e) $N_2(A)$ density (1/m^3); (f) $N_2(C)$ density (1/m^3).

and at the reactor walls, but the temperature above the substrate is relatively uniform around 130 °C. A maximum wall temperature of 230 °C is reached close to the electrodes. Attention has to be paid not to overheat the reactor wall, as experimentally experienced with a reactor made of polymer. Note that with the calculated electron density of the order of 10^{20} m^{-3}, plasma heating may be non-negligible and the model should be extended to account for this effect.

6. Conclusions

Complex flow patterns have to be accounted for when simulating atmospheric-pressure plasma reactors. Coupling computational fluid dynamics with the calculation of the electric field and the plasma chemistry is challenging due to the numerical stiffness resulting from the strongly different time scales of the phenomena involved. Considering low-temperature, atmospheric-pressure pure nitrogen plasma, a model and solution strategy are presented to make coupled simulations computationally tractable. 21 reactions are considered, including direct excitation, ionization and dissociation of background nitrogen, relaxation of excited states through radiative processes and collisions with neutrals, recombination of electrons and ions and charge transfer. Photo-ionization is not accounted for. The numerical stiffness is strongly reduced by using the Poisson equation for the calculation of the electric field and applying the quasi-steady state approximation for short-lived species and this without significantly affecting the accuracy of the solution of the model used. Solving the Boltzmann equation is avoided by using solutions provided by the BOLSIG+ solver to derive correlations for the electron mean energy as a function of the reduced electric field, as well as for the electrical mobility and diffusivity of the electrons. Simulations remain, however, challenging due to extremely strong spatial gradients in the electric and species concentration fields, in particular near the electrodes. To evaluate the approach, 2D simulations of a sharp-end plate-to-plane configuration and of a specific pilot-scale low-temperature, atmospheric-pressure plasma enhanced chemical vapor deposition (APPECVD) reactor prototype were presented, imposing a 5 kV potential between the electrodes. Both Penning ionization and secondary emission are seen to be important to sustain a discharge. When neglecting secondary emission or at a higher imposed potential when electrons are rapidly lost, a discharge could not be sustained. Explicitly accounting for photo-ionization or artificially increasing secondary emission can be considered. The bulk flow generated by a discharge is seen to be significant and complex. Vortices are generated and velocities attain locally several meters per second. The flow field largely determines the observed electron and species

concentration fields, directly for long-lived species and indirectly for short-lived species if their concentration depends on the concentrations of long-lived species. The simulations clearly illustrate the importance of accounting for complex flow dynamics to understand the performance and scale-up of atmospheric pressure plasma reactors. Extension of the model to account for plasma heating may be required in certain cases.

References

Armaou A and Christofides P D 1999 Plasma enhanced chemical vapor deposition: modeling and control *Chem. Eng. Sci.* **54** 3305–14

Aubry O, Met C, Khacef A and Cormier J M 2005 On the use of a non-thermal plasma reactor for ethanol steam reforming *Chem. Eng. J.* **106** 241–7

Bak M S, Kim W and Cappelli M A 2011 On the quenching of excited electronic states of molecular nitrogen in nanosecond pulsed discharges in atmospheric pressure air *Appl. Phys. Lett.* **98** 011502

Bardina J E, Huang P G and Coakley T J 1997 Turbulence modeling validation, testing and development *NASA Technical Memorandum* p 110446

Barranco A, Cotrino J, Yubero F, Espinós J P, Benítez J, Clerc C and Gonzáles-Elipe A R 2001 Synthesis of SiO_2 and $SiO_xC_yH_z$ thin films by microwave plasma CVD *Thin Solid Films* **401** 150–8

Baudrez E, Heynderickx G J and Marin G B 2010 Steady-state simulation of fluid catalytic cracking riser reactors using a decoupled solution method with feedback of the cracking reactions on the flow *Chem. Eng. Res. Des.* **88** 290–303

Benilov M S and Naidis G V 2003 Modelling of low-current discharges in atmospheric-pressure air taking account of non-equilibrium effects *J. Phys. D: Appl. Phys.* **36** 1834

Bogaerts A, Neyts E, Gijbels R and van der Mullen J 2002 Gas discharge plasmas and their applications *Spectrochim. Acta* B **57** 609–58

Bogaerts A, De Bleecker K, Georgieva V, Kolev I, Madani M and Neyts E 2006 Computer simulations for processing plasmas *Plasma Process. Polym.* **3** 110–9

Brandenburg R, Maiorov V A, Golubovskii Yu B, Wagner H-E, Behnke J and Behnke J F 2005 Diffuse barrier discharges in nitrogen with small admixtures of oxygen: discharge mechanism and transition to the filamentary regime *J. Phys. D: Appl. Phys.* **38** 2187

Breden D, Miki K and Raja L L 2012 Self-consistent two-dimensional modeling of cold atmospheric-pressure plasma jets/bullets *Plasma Sources Sci. Technol.* **21** 034011

Breden D and Raja L L 2014 Computational study of the interaction of cold atmospheric helium plasma jets with surfaces *Plasma Sources Sci. Technol.* **23** 065020

Cheimarios N, Kokkoris G and Boudouvis A G 2010 Multiscale modeling in chemical vapor deposition processes: coupling reactor scale with feature scale computations *Chem. Eng. Sci.* **65** 5018–28

Chen J and Davidson J H 2002 Electron density and energy distributions in the positive DC corona: interpretation for corona-enhanced chemical reactions *Plasma Chem. Plasma Process.* **22** 199–224

Choi Y H, Kim J H and Hwang Y S 2006 One-dimensional discharge simulation of nitrogen DBD atmospheric pressure plasma *Thin Solid Films* **506–7** 389–95

De Bie C, Verheyde B, Martens T, van Dijk J, Paulussen S and Bogaerts A 2011 Fluid modeling of the conversion of methane into higher hydrocarbons in an atmospheric pressure dielectric barrier discharge *Plasma Process. Polym.* **8** 1033–58

Descamps P, Kaiser V, Asad S S and Leempoel P 2011 Study of the kinetics of droplets size evolution and the mechanisms of solid particles creation in an atmospheric plasma jet, using a laser beam diffraction technique *Plasma Process. Polym.* **8** 1116–25

Descamps P, Asad S S and De Wilde J 2013 Atmospheric-pressure plasma enhanced chemical deposition: role of the reactor flow dynamics *J. Phys. D: Appl. Phys.* **46** 365201

Ellis H W, McDaniel E W, Albritton D L, Viehland L A, Lin S L and Mason E A 1978 Transport properties of gaseous ions over a wide energy range *At. Data Nucl. Data Tables* II **22** 179–217

Enache I, Caquineau H, Gherardi N, Paulmier T, Maechler L and Massines F 2007 Transport phenomena in an atmospheric-pressure townsend discharge fed by N_2/N_2O/HMDSO mixtures *Plasma Process. Polym.* **4** 806–14

Foest R, Adler F, Sigeneger F and Schmidt M 2003 Study of an atmospheric pressure glow discharge (APG) for thin film deposition *Surf. Coat. Technol.* **163–4** 323–30

Froment G F, Bischoff K B and De Wilde J 2010 *Chemical Reactor Analysis and Design* 3th edn (New York: Wiley)

Gadonna K, Leroy O, Silva T, Leprince P, Boisse-Laporte C and Alves L L 2011 Hydrodynamic study of a microwave plasma torch *Eur. Phys. J. Appl. Phys.* **56** 24008

Gaudi T, Iacono J, Toutant A, Descamps P, Leempoel P and Massines F 2011 Role of confinement in the development of a helium impacting plasma jet at atmospheric pressure *20th Conf. on Plasma Chemistry* (*Philadelphia, USA*)

Golubovskii Yu B, Maiorov V A and Behnke J F 2002 Influence of interaction between charged particles and dielectric surface over a homogeneous barrier discharge in nitrogen *J. Phys. D: Appl. Phys.* **35** 751

Golubovskii Y B, Maiorov V A, Behnke J and Behnke J F 2005 On the homogeneity of the glow-like barrier discharge at atmospheric pressure *Plasma Process. Polym.* **2** 188–92

Hagelaar G J M and Kroesen G M W 2000 Speeding up fluid models for gas discharges by implicit treatment of the electron energy source term *J. Comput. Phys.* **159** 1–12

Hagelaar G J M and Pitchford L C 2005 Solving the Boltzmann equation to obtain electron transport coefficients and rate coefficients for fluid models *Plasma Sources Sci. Technol.* **14** 722–33

Hoekstra R J and Kushner M J 1998 Comparison of two-dimensional and three-dimensional models for profile simulation of poly-Si etching of finite length trenches *J. Vacuum Sci. Technol.* A **16** 3274–80

Huxley L G H and Crompton R W 1974 *The Diffusion and Drift of Electrons in Gases* (New York: Wiley)

Itikawa Y 2006 Cross sections for electron collisions with nitrogen molecules *J. Phys. Chem. Ref. Data* **35** 31

Jayaraman B and Shyy W 2008 Modeling of dielectric barrier discharge-induced fluid dynamics and heat transfer *Prog. Aerosp. Sci.* **44** 139–91

Jayatilleke C L V 1969 The influence of Prandtl number and surface roughness on the resistance of the laminar sublayer to momentum and heat transfer *Prog. Heat Mass Trans.* **1** 193–329

Kleijn C R, Dorsman R, Kuijlaars K J, Okkerse M and van Santen H 2007 Multi-scale modeling of chemical vapor deposition processes for thin film technology *J. Cryst. Growth* **303** 362–80

Kossyi I A, Kostinsky A Yu, Matveyev A A and Silakov V P 1992 Kinetic scheme of the non-equilibrium discharge in nitrogen-oxygen mixtures *Plasma Sources Sci. Technol.* **1** 207–20

Kushner M K 2009 Hybrid modelling of low temperature plasmas for fundamental investigations and equipment design *J. Phys. D: Appl. Phys.* **42** 194013

Launder B E and Spalding D B 1972 *Mathematical Models of Turbulence* (New York: Academic)

Lin K-M, Hung C-T, Hwang F-N, Smith M R, Yang Y-W and Wu J-S 2012a Development of a parallel semi-implicit two-dimensional plasma fluid modeling code using finite-volume method *Comput. Phys. Commun.* **183** 1225–36

Lin K-M, Hu M-H, Hung C-T, Wu J-S, Hwang F-N, Chen Y-S and Cheng G 2012b A parallel hybrid numerical algorithm for simulating gas flow and gas discharge of an atmospheric-pressure plasma jet *Comput. Phys. Commun.* **183** 2550–60

Lorant C 2013 2D model of an atmospheric pressure plasma deposition reactor *MSc Thesis* Université catholique de Louvain (UCL), Louvain-la-Neuve

Lozano-Parada J H and Zimmerman W B 2010 The role of kinetics in the design of plasma microreactors *Chem. Eng. Sci.* **65** 4925–30

Martins A A 2013 Modelling of an improved positive corona thruster and actuator *J. Electrost.* **71** 61–7

Massines F, Gherardi N, Fornelli A and Martin S 2005 Atmospheric pressure plasma deposition of thin films by Townsend dielectric barrier discharge *Surf. Coat. Technol.* **200** 1855–61

Massines F, Gherardi N, Naudé N and Ségur P 2008 Recent advances in the understanding of homogeneous dielectric barrier discharges *11th Int. Symp. on High Pressure, Low Temperature Plasma Chemistry (Hakone XI) (Oléron Island, France, 7–12 September 2008)*

Moreau E 2004 Airflow control by non-thermal plasma actuators *J. Phys. D: Appl. Phys.* **40** 605–36

Petrovic D, Martens T, van Dijk J, Brok W J M and Bogaerts A 2009 Fluid modelling of an atmospheric pressure dielectric barrier discharge in cylindrical geometry *J. Phys. D: Appl. Phys.* **42** 205206

Punjabi S B, Sahasrabudhe S N, Ghorui S, Das A K, Joshi N K, Kothari D C, Ganguli A A and Joshi J B 2014 Flow and temperature patterns in an inductively coupled plasma reactor: Experimental measurements and CFD simulations *AIChE J.* **60** 3647–64

Radmilovic M, Radjenovic B and Kals M 2014 The breakdown phenomena in micrometer scale direct-current gas discharge *Plasma Chem. Plasma Process.* **34** 55–64

Ravasio S and Cavallotti C 2012 Analysis of reactivity and energy efficiency of methane conversion through non thermal plasmas *Chem. Eng. Sci.* **84** 580–90

Reece Roth J 1995 *Industrial Plasma Engineering* (*Principles* vol 1) (Boca Raton, FL: CRC Press)

Schütze A, Jeong J Y, Babayan S E, Park J, Selwyn G S and Hicks R F 1998 The atmospheric-pressure plasma jet: a review and comparison to other plasma sources *IEEE Trans. Plasma Sci.* **26** 1685–94

Tendero C, Tixier C, Tristant P, Desmaison J and Leprince P 2006 Atmospheric pressure plasmas: areview *Spectrochim. Acta* B **61** 2–30

Van Gaens W and Bogaerts A 2013 Kinetic modelling for an atmospheric pressure argon plasma jet in humid air *J. Phys. D: Appl. Phys.* **46** 275201

Viehland L A and Mason E A 1995 Transport properties of gaseous ions over a wide energy range *At. Data Nucl. Data Tables IV* **60** 37–95

Wilcox D C 2006 *Turbulence Modeling for CFD* 3th edn (La Cañada Flintridge, CA: D C W Industries)

Xiong Z, Robert E, Sarron V, Pouvesle J-M and Kushner M J 2013 Atmospheric-pressure plasma transfer across dielectric channels and tubes *J. Phys. D: Appl. Phys.* **46** 155203

Zakari M, Caquineau H, Hotmar P and Segur P 2015 An axisymetric unstructured finite volume method applied to the numerical modeling of an atmospheric pressure gas discharge *J. Comput. Phys.* **281** 473–92